Hindawi
Concepts in Magnetic Resonance Part A, Bridging Education and Research
Volume 2022, Article ID 8709075, 10 pages
https://doi.org/10.1155/2022/8709075

Research Article

Deep Learning-Based Magnetic Resonance-Ultrashort Time of Echo Imaging for Analyzing Degeneration of Intervertebral Disc Cartilage Endplate and Rehabilitation Nursing

Sainan Jiang,[1] **Xiaoyun Song**,[1] **and Chengming Jiang**[2]

[1]*Department of Science and Education, The First Hospital of Changsha, Changsha 410005, Hunan, China*
[2]*Department of Spine Surgery, The First Hospital of Changsha, Changsha 410005, Hunan, China*

Correspondence should be addressed to Chengming Jiang; 202111120911186@zcmu.edu.cn

Received 25 April 2022; Revised 9 June 2022; Accepted 22 June 2022; Published 13 July 2022

Academic Editor: Enas Abdulhay

This study was focused on the magnetic resonance-ultrashort time of echo (MR-UTE) imaging technology based on the convolution residual network (CRN) algorithm to evaluate the degeneration of intervertebral disc endplate (DIDCE) and the efficacy of rehabilitation nursing intervention. In this study, 90 patients with intervertebral disc degeneration in the hospital were randomly divided into an intervention group (45 cases) and a control group (45 cases). All patients were scanned by a magnetic resonance imaging system, and the original UTE images were postprocessed. The control group received routine nursing. The intervention group used massage and rehabilitation nursing intervention measures. The CRN algorithm is used to reconstruct the undersampled MR image and compared with ESPIRiT algorithm and the Regridding algorithm. The result found that CRN has more advantages than ESPIRiT and Regridding reconstruction algorithms. The proportion of partial disappearance and complete disappearance of fibrous ring structure in the low back pain group was higher than that in the non-low back pain group, with a statistical difference ($P < 0.05$). 90 patients with intervertebral disc cartilage endplate degeneration were divided into lumbago group (62 cases) and nonlumbago group (28 cases) according to whether they had lumbago. The nursing satisfaction of patients in the intervention group (97%) is significantly higher than that of patients in the control group (69%) ($P < 0.05$). In conclusion, the CRN algorithm successfully removes artifacts and noise in the undersampled image. Cartilage endplate, annulus fibrosus, and bony endplate partially disappeared by the MR-UTE imaging technique. Rehabilitation intervention proved to have a positive effect on the treatment of patients with intervertebral disc degeneration and can improve patients' satisfaction.

1. Introduction

The intervertebral disc is a fibrous cartilaginous structure that connects the adjacent vertebrae of the spine and consists of a central nucleus pulposus and the surrounding annulus fibrosus. It is located within the boundary of the intervertebral space. The upper and lower boundaries of the intervertebral space are the endplate of the vertebral body, and the surrounding boundaries of the intervertebral space are the plane of the bony edge of the spine [1, 2]. The main function of the disc is to bear the pressure, load the flexibility and elasticity of the spine, and cushion the shock. Degeneration of intervertebral disc endplate (DIDCE) arises from the natural aging of the body and the joint action of various factors. It manifests as a series of cascade reactions in various parts of the cartilage endplate of the intervertebral disc under various mechanisms of action such as pathophysiology, biochemistry, and biomechanics [3–5]. DIDCE is a prerequisite and pathological basis for spinal degenerative osteoarthropathy and is one of the main causes of low back pain.

With the development of imaging technology, the main methods for clinical examination of the lumbar spine include *X*-ray, CT examination, and magnetic resonance (MR) [6]. *X*-ray examination is the most commonly used imaging examination in clinical practice, which is simple and of low cost, but cannot directly show the internal structure of the intervertebral disc [7]. CT examination has obvious

advantages in the bone examination due to its short scanning time and high-density resolution, but its soft tissue contrast is poor and it cannot display the structure of cartilage endplate and annulus fibrosus [8]. MR has the advantages of no radiation, high soft tissue resolution, and no overlapping image, showing great potential in the morphology and functional display of intervertebral disc and becoming the main imaging examination method of the lumbar spine [9–12]. With the continuous progress of imaging technology, magnetic resonance-ultrashort time of echo (MR-UTE) technology can significantly shorten the echo time and collect and display short T2 tissue signals, pointing out a new research path for DIDCE [13]. The MR-UTE double-echo sequence can directly display the cartilage endplate, improve the intertissue contrast of the vertebral disc junction area, and visually distinguish the annulus fibrosus, cartilage endplate, and bone endplate, facilitating the comparison of DIDCE imaging with conventional MR sequences [14].

As a data-oriented processing method, deep learning can classify and segment common features among complex training data sets. In addition, deep learning is widely used in image deblurring, denoising, and image enhancement. In this study, the convolution residual network (CRN) algorithm was constructed to learn the mapping relationship between undersampled and fully-sampled MRI images. Then, it was required to predict the signals lacking in undersampled images to obtain approximately fully-sampled MRI images [15, 16].

In this study, 90 patients with intervertebral disc cartilage endplate degeneration were selected, and all of them underwent MR-UTE examination. The MR-UTE images of patients were processed by constructing a convolution residual network algorithm, aiming at analyzing whether low back pain will cause the difference in the degenerative intervertebral disc and whether it will affect the morphological structure and distribution of annulus fibrosus, cartilage endplate, and bony endplate, so as to provide an earlier and more accurate diagnosis basis for the clinic.

2. Materials and Methods

2.1. Subjects. In this study, 90 DIDCE patients enrolled in the hospital from November 20, 2019, to December 20, 2020, were divided into an intervention group (45 cases) and a control group (45 cases) according to the presence or absence of low back pain, with a total of 450 discs. There were 35 males and 55 females, aged 25–75 years, with an average weight of 51.26 ± 12.64 kg. There was no significant difference in general data between the two groups ($P > 0.05$), indicating comparability. This study had been approved by the ethics committee of the hospital, and patients and their families signed the informed consent form.

Inclusion criteria are as follows: (1) conventional MRI showed different degrees of lumbar disc degeneration; (2) patients with previous lumbosacral stiffness or pain are included; (3) MRI imaging data were complete.

Exclusion criteria are as follows: (1) patients with previous infections, diseases of the blood system, and metabolic diseases; (2) history of spinal surgery, spinal malformation surgery, spinal trauma, etc.; (3) with claustrophobia, IUDS, spinal metal implantation, early pregnancy, and other MRI scan contraindications.

2.2. MR-UTE Examination. All patients were examined by a 3.0 T magnetic resonance imaging system, using the whole spine coil. The patient was in a supine position, with the head advanced, at the level of the third lumbar spine. The entire lumbar spine was scanned, ranging from the T12/L1 to the L5/S1 discs. Each patient underwent a conventional sagittal scan with T1WI, T2WI, and UTE double-echo sequences. Table 1 showed the scan sequence parameters.

2.3. Construction of CRN Algorithm. As an important technique to interpolate nonuniformly sampled data points into a straight line grid, the gridding algorithm has been widely researched and innovated. The improved gridding algorithm is defined as the gridding algorithm, which is used for MR image reconstruction in experiments.

The Kaiser-Bessel function used by the Jackson gridding algorithm is

$$\left\{ \begin{array}{ll} \omega(\lambda) = \dfrac{I_0\left(\alpha\sqrt{1-(2\lambda/W)^2}\right)}{I_0(\beta)}, & |\lambda| \le \dfrac{W}{2} \\ \omega(\lambda) = 0, & |\lambda| > \dfrac{W}{2} \end{array} \right\}, \quad (1)$$

where (λ) is the Kaiser-Bessel window function, I_0 is the zero-order modified Bessel function, and W is the window length.

The calculation formula of the MRI image finally reconstructed by the gridding algorithm is

$$M_i(x, y) = M_r(x, y) \cdot \frac{f(x, y)}{r(x, y)}, \quad (2)$$

where M_i is the reconstructed MRI image, M_r is the inverse Fourier transform of, f is the inverse Fourier transform of, and r is a rectangular function.

To improve the accuracy under undersampling technical conditions, this study proposes a deep learning-based artifact removal method, the CRN algorithm. Firstly, the undersampled MR image is reconstructed and processed using the following equation.

$$\mathrm{MR}_{\text{high quality}} = F\left(\mathrm{MR}_{\text{low quality}}\right), \quad (3)$$

where $\mathrm{MR}_{\text{low quality}}$ represents the MR image reconstructed from undersampled data, which contains a large number of noise points and artifacts. $\mathrm{MR}_{\text{high quality}}$ represents the MR image reconstructed from fully sampled data, used as the gold standard for image reference. F function, learned by CNN, is used to process undersampled MR images with artifacts and noise.

There are mainly three steps. First, MR data of full sampling and undersampling are obtained by 3D-UTE

Table 1: The scan parameters of T1WI, T2WI, and UTE.

	T1WI	T2WI	UTE
Repetition time (ms)	450	4200	87.3
Time of echo 1 (ms)	20	120	0.029
Time of echo 2 (ms)	—	—	7.2
Flip angle	90°	90°	15°
Layer thickness (mm)	2.5	2.5	2.5
Layer spacing (mm)	1	1	1
Matrix	385 × 258	385 × 258	512 × 512
Number of layers	16	16	32
Echo train length	9	25	—
Scanning time	136 s	110 s	506 s
Number of excitation	1.5	1	1

sequence acquisition, and a reconstruction algorithm is used to reconstruct the image, with the full sampling MR image taken as the gold standard. Then, a three-layer neural network is constructed and trained with undersampled and fully sampled image data at different echo times, so that it can effectively remove the noise and artifacts from undersampled images [17, 18]. Finally, the CRN algorithm is used to predict MR images of high quality. The structure diagram of the CRN algorithm is shown in Figure 1.

The CRN algorithm is calculated as follows.

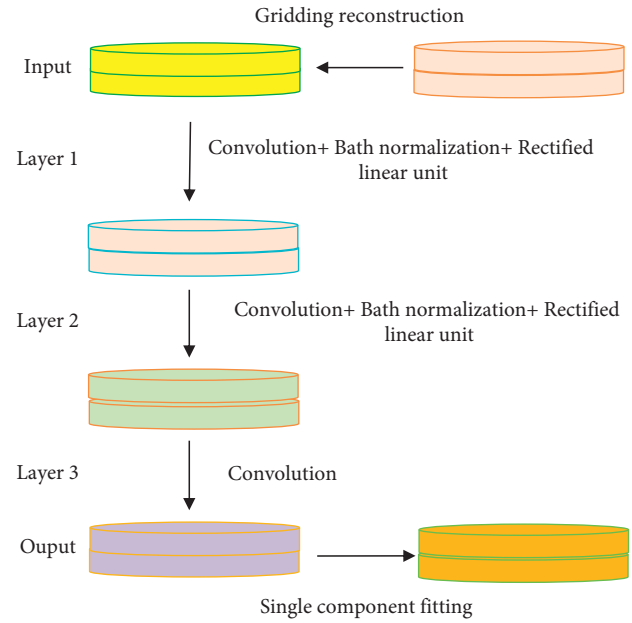

Figure 1: Schematic diagram of the structure of the CRN algorithm.

$$M_0 = M_i + W_1 \times \mathrm{RO}\left(\mathrm{ReLU}\left(W_2 \times \mathrm{RO}\left(\mathrm{ReLU}\left(W_2 \times M_i + a_1\right)\right) + a_2\right)\right) + a_3, \tag{4}$$

where M_i represents the undersampled MR image whose undersampled multiple is 2; W_1, W_2, and W_1 all represent the weight, which contains the convolution kernel of 5×5; a_1, a_2, and a_3 represent the bias quantity, ReLU represents the activation function, and RO represents the normalization operation. The loss function is expressed as follows.

$$L(A, B) = \frac{1}{N} \times \sum_{j=1}^{N} \left|A_i - B_i\right|, \tag{5}$$

where A_i represents pixels in the undersampled MR image, B_i represents B_i pixels in the fully sampled MR image, and A_i and B_i correspond to each other. $L(A, B)$ represents the loss function, and N represents the number of pixels in the MR image.

2.4. MR-UTE Image Postprocessing and Data Measurement. After the scanning, the UTE original image was postprocessed. First, the original UTE images of each patient were uploaded to the workstation under the same repetition time and different echo times. The image positions were consistent at each echo time, and the two groups of images with the same number of layers at each echo time were silhouetted by postprocessing software. The original image of the second layer echo time was subtracted from the original image of the first layer echo time, the image after silhouette was retained, and the original image of the first echo time was saved.

The sharpness of anatomical structures in T1WI, T2WI, and UTE images was compared semiquantitatively with conventional MR sequences, and the articulation of intervertebral disc and surrounding structures, annulus fibrosus (AF), cartilage end plate (CEP), and vertebral end plate (VEP) was assessed.

2.5. Imaging Indicators of DIDCE. At present, the Pfirrmann grading method is commonly used clinically (Table 2) [19], which often requires sagittal images of the T2WI sequence for diagnosis. Two physicians independently evaluated the degeneration signs of each intervertebral disc segment, and any inconsistency was solved through consultation and discussion.

2.6. Sagittal Double-Echo MR-UTE Image. The MR-UTE was used to analyze the cartilaginous endplates, annulus fibroids, and vertebral endplates in DIDCE patients: complete, partially absent, and completely absent according to their structural integrity. Integrity refers to the continuity of structural morphology observed at all sagittal levels; partial disappearance refers to the continuous interruption of structural signals at two consecutive levels observed at the sagittal level, and the interruption length is less than half of the transverse diameter of the structure; complete disappearance refers to the continuous interruption of the structural signal from the sagittal plane, and the interruption length reaches more than half of the transverse diameter of

Table 2: DIDCE Pfirrmann grading.

Characteristics	Grade I	Grade II	Grade III	Grade IV	Grade V
Structure of nucleus pulposus	Even, bright white	Uneven, horizontal band can be observed	Uneven, gray	Uneven, gray to black	Uneven, black
Nucleus pulposus-annulus fibrosus boundary	Clear	Clear	Unclear	Lost	Lost
Nucleus pulposus signal intensity	High (comparable to cerebrospinal fluid)	High (comparable to cerebrospinal fluid)	Medium	Medium to low	Low
Disc height	Normal	Normal	Slightly reduced	Moderately reduced	Severely reduced

the structure. Two physicians read the films independently. Any disagreement was solved through consultation and discussion. The imaging findings should be observed, recorded, and counted.

2.7. Rehabilitation Nursing Intervention Methods. The control group received routine nursing. In the intervention group, on the basis of routine nursing, massage and rehabilitation nursing intervention measures were used, and the patients' waist acupoints were professionally massaged. At the same time, health education, rehabilitation nursing, rehabilitation training, and retraining were given to the patients. Rehabilitation nursing intervention is as follows.

Monitoring of respiration, blood pressure, blood oxygen saturation, and electrocardiogram: all patients in this group had different degrees of anemia after the operation, and extubation was delayed for 16 hours after anesthesia. After the patient returned to the ward, he was given 3 L/min of oxygen, monitored by bedside ECG, and closely monitored pulse, respiration, blood pressure, oxygen saturation, and ECG. Observe and record every 30 min minutes within 6 hours after the operation, and change to 1 hour after stabilization until 48 hours or 72 hours. After treatment and nursing, he was discharged from the hospital.

And the monitoring of spinal cord and nerve function: make the patient move both lower limbs, and evaluate whether the muscle strength is back to normal. Observe and record every 30 minutes in the first 12 hours after operation to prevent the occurrence of spinal cord ischemia-reperfusion injury.

Comprehensive functional exercise: on the day of operation, encourage and assist patients to stretch and bend their ankles and knees, improve the muscle fatigue of supine limbs, and relax muscles after operation and operation. On the first day after the operation, respiratory function training was added, and the frequency and intensity of training were determined according to the patient's personal tolerance and the patient's basic exercise. On the third day after the operation, the exercise of both upper limbs was increased, including fist-clenching, chest-expanding, shoulder-shrugging, shoulder-lifting, abduction, and rotation, so as to promote the recovery of vital capacity and prevent scapulohumeral periarthritis and joint stiffness. One week after the operation, after the patient's body temperature dropped, pain improved, and physique recovered, four-point support training was conducted to train the back extension function.

2.8. Statistical Methods. SPSS 21.0 statistical software was used for the statistical analysis of the data. The calculated data conforming to normal distribution were represented by the mean standard deviation ($\overline{X} \pm S$) and the T-test was adopted. The in-conforming data were expressed as the percentage (%) and the χ^2 test was used. The structural integrity and distribution of cartilage end plate, annulus fibrosus, and osseous end plate at different DIDCE levels were examined by $R \times C$ chi-square. Kendall's rank correlation was used to analyze the correlation of dichotomous variables. $P < 0.05$ indicated significant differences.

3. Results

3.1. Experimental Results of Different Algorithms. Select the region of interest (ROI) in the experiment; an MR image reconstructed from full sampling data is the gold standard of the image reference. The Regridding algorithm, ESPIRiT algorithm, and CRN algorithm were used to reconstruct MR images, respectively. Then, the 10 echo signals of single exponential fitting were compared with the gold standard for F-test, to judge whether the fitting results obtained by the three algorithms were significantly different from the gold standard.

As shown in Figure 2, the 10 echo signals of ESPIRiT algorithm and CRN algorithm had higher numerical similarity with gold standard echo signals, and the attenuation trend of echo signals was more similar to the gold standard. According to Figure 3, the reconstruction results of the Regridding algorithm were statistically different from the gold standard, while the results of ESPIRiT algorithm and CRN algorithm were not significantly different from the gold standard. Compared with ESPIRiT reconstruction algorithm, the CRN reconstruction algorithm had more advantages.

3.2. UTE Imaging Analysis of Bone Integrity of Cartilage Endplate, Annulus Fibrosus, and Vertebral Endplate. In the UTE image in the first echo signal, the nucleus pulposus showed a uniform low signal; the cartilaginous endplate between the nucleus pulposus and the upper and lower vertebral bodies showed continuous high signal; the vertebral endplate showed continuous and complete isosignal; the annulus fibrosus of the nucleus pulposus had a spindle shape and slightly higher signal. After the UTE image was silhouetted, the nucleus pulposus still showed uniform low

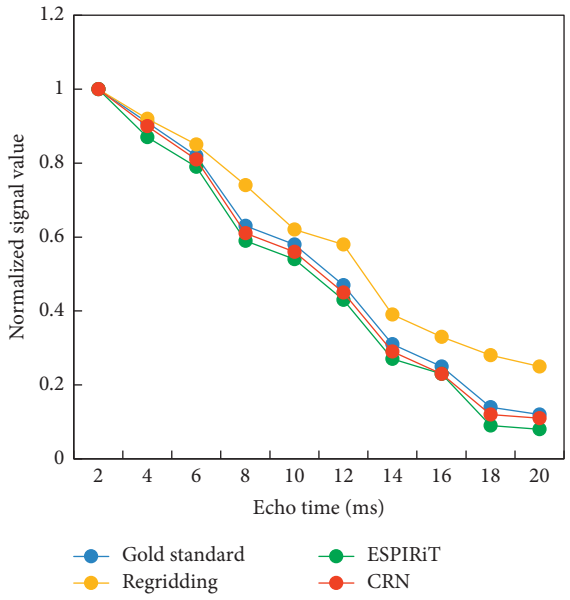

Figure 2: Line chart of 10 echo signals of Regridding, ESPIRiT, and CRN algorithms.

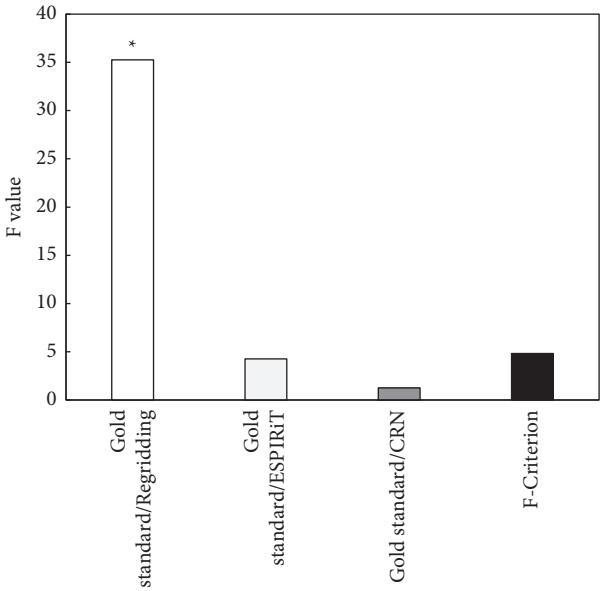

Figure 3: *F*-test results of Regridding, ESPIRiT, and CRN algorithms. *Compared with *F*-standard, $P < 0.05$.

signal; the cartilaginous endplate showed linear continuous high signal; the upper and lower layers of the vertebral endplate were intact and continuous, presenting slightly low signal; the annulus fibrosus was complete in shape, and the signal was continuously slightly higher (Figure 4).

The UTE images of moderate DIDCE in the first echo signal and after silhouette showed that the morphological structure of the cartilage endplate, annulus fibrosus, and vertebral endplate was partially disappeared and that the structure of one side was incomplete (Figure 5).

The UTE images of severe DIDCE in the first echo signal and after silhouette showed that the morphological structure of the cartilage endplate, annulus fibrosus, and vertebral endplate was absent and that the structures of the upper and lower sides were absent (Figure 6).

3.3. Bone Integrity Distribution and Composition Ratio of Cartilage Endplate, Annulus Fibrosus, and Vertebral Endplate. 90 patients with intervertebral disc cartilage endplate degeneration were divided into the lumbago group (62 cases) and nonlumbago group (28 cases) according to whether they had lumbago. The bone integrity of the cartilaginous endplate and bony endplate structure showed no statistical difference between the two groups ($P > 0.05$). They had the highest proportion of partial disappearance and the lowest proportion of complete disappearance in both groups. As for the structural integrity distribution of annulus fibrosus, the proportions of partial disappearance and complete disappearance were higher in the lumbago group than in the nonlumbago group, with statistical differences ($P < 0.05$), as shown in Figure 7.

3.4. Correlation Analysis between Clinical Symptoms and Degeneration Degree of Intervertebral Disc. Included discs were graded according to the Pfirrmann grading criteria, as shown in Figure 8. Patients were divided into lumbago group and nonlumbago group according to the clinical symptoms, and there was no statistical difference in the constituent ratio between the two groups ($P > 0.05$), indicating that there was little correlation between the intervertebral disc degeneration degree and clinical symptoms.

3.5. The Correlation between Structural Integrity of Cartilage Endplate and Pfirrmann Grading of Intervertebral Disc Degeneration. According to the different Pfirrmann grades of the lumbago group and the nonlumbago group, the $R \times C$ Chi-square test was performed on the integrity composition ratio of different cartilage endplates. The results showed that the χ^2 of the lumbago group and the nonlumbago group were 169.32 and 35.02, respectively, with a statistical difference ($P < 0.05$), indicating that intervertebral disc degeneration was correlated with the integrity of cartilage endplate. Kendall's was 0.512 and 0.547, respectively, showing a moderate correlation (Tables 3–4).

3.6. Satisfaction of Rehabilitation Nursing. The experimental results show that the nursing satisfaction of patients in the intervention group (97%) is significantly higher than that of patients in the control group (69%), and there is a statistical difference between the two groups ($P < 0.05$) (Figure 9).

4. Discussion

With a series of physiological and pathological changes, the internal permeability of the intervertebral disc nucleus pulposus reduces, and water loss gradually occurs, leading to fibrosis, and then nucleus pulposus tension is falling and intervertebral disc height changes, resulting in a material exchange between the cartilage endplate in dispersion effect.

(a) (b) (c)

Figure 4: T2WI, T1WI, and UTE images of a female aged 53 who did not have low back pain. (a) T2WI; (b) T1WI; (c) UTE.

(a) (b) (c)

Figure 5: T2WI, T1WI, and UTE images of a male aged 65 who had suffered low back pain accompanied by radiating pain in the left limb for 5 years. (a) T2WI; (b) T1WI; (c) UTE.

Therefore, cartilage endplate degeneration is a major cause of intervertebral disc degeneration. MR imaging manifestations of intervertebral disc degeneration mainly include decreased T2 signal of the intervertebral disc, intervertebral disc vacuum changes, bone marrow changes, mutations, annulus fibrosus tears, calcification, ligament changes, and spinal stenosis [20–22]. Decreased disc T2 signal is due to changes in glycosaminoglycan concentration and water molecular content. As the disc develops, a vacuum will occur, which on MR imaging shows no signal on T1WI and

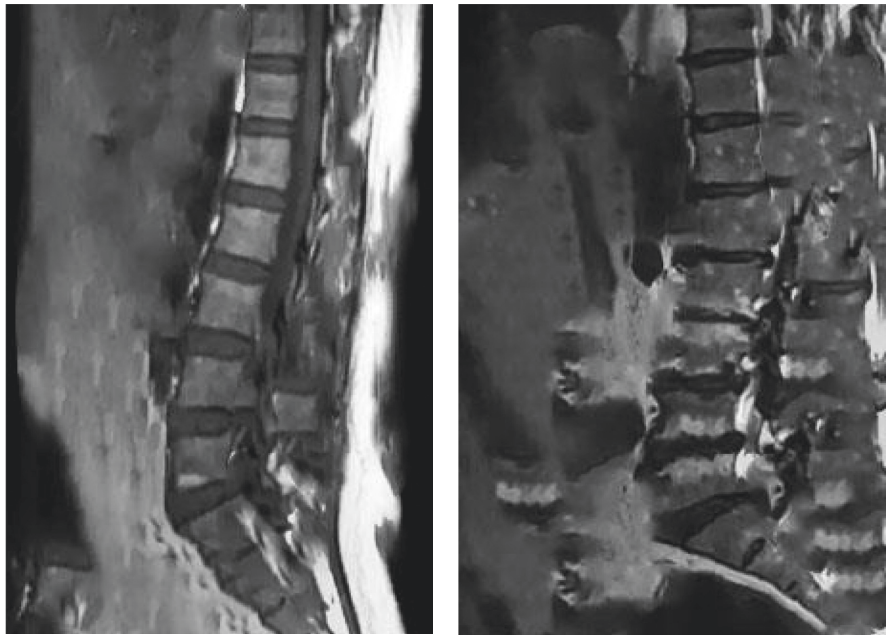

(a) (b)

Figure 6: T2WI and UTE images of a female aged 62 who had suffered repeated low back pain for 8 years. (a) T2WI; (b) UTE.

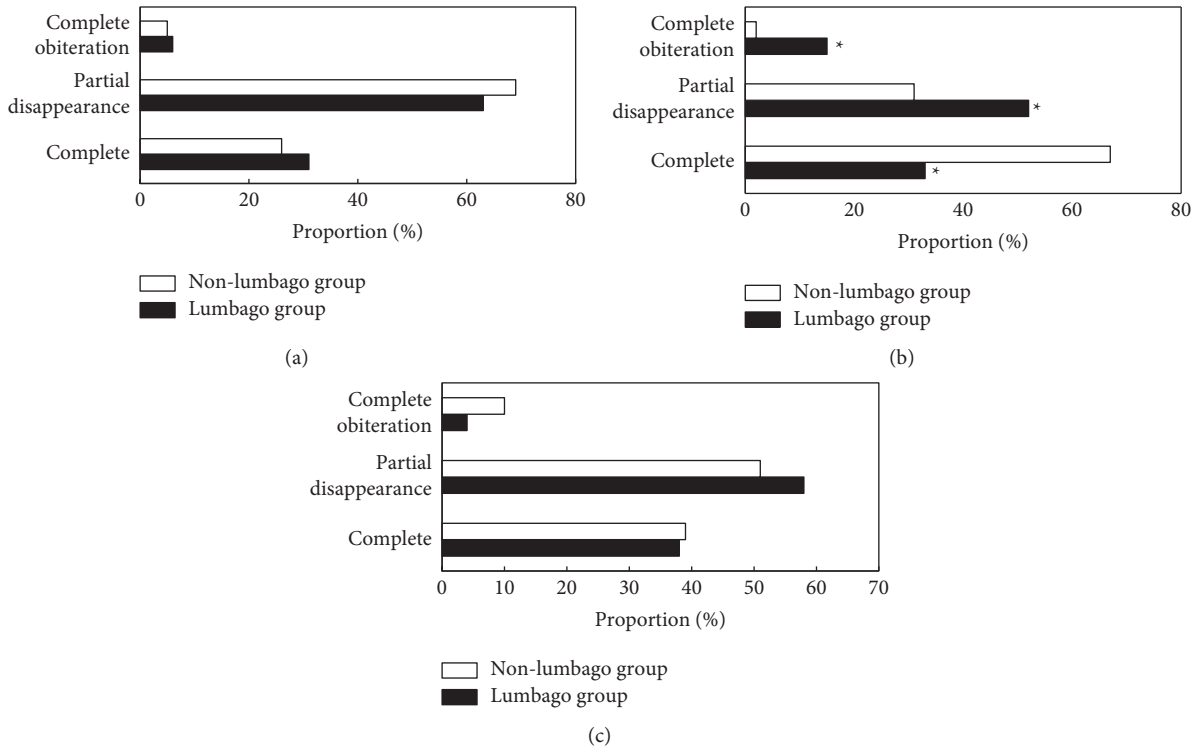

Figure 7: Bone integrity analysis of cartilage endplate, annulus fibrosus, and vertebral endplate. (a) Integrity of cartilage endplate; (b) annulus fibrous integrity; (c) integrity of vertebral endplates. *Compared with the nonlumbago group, $P < 0.05$.

T2WI images. When the intervertebral disc is calcified, there will be a low signal or no signal in the MR image. Pfirrmann grading scale is a T2WI sagittal grading method based on intervertebral disc nucleus pulposus structure, signal strength, intervertebral disc height, and annulus fibrosus boundary.

MR-UTE technology is a new technology for short T2 tissue imaging in the human body, which can reduce the

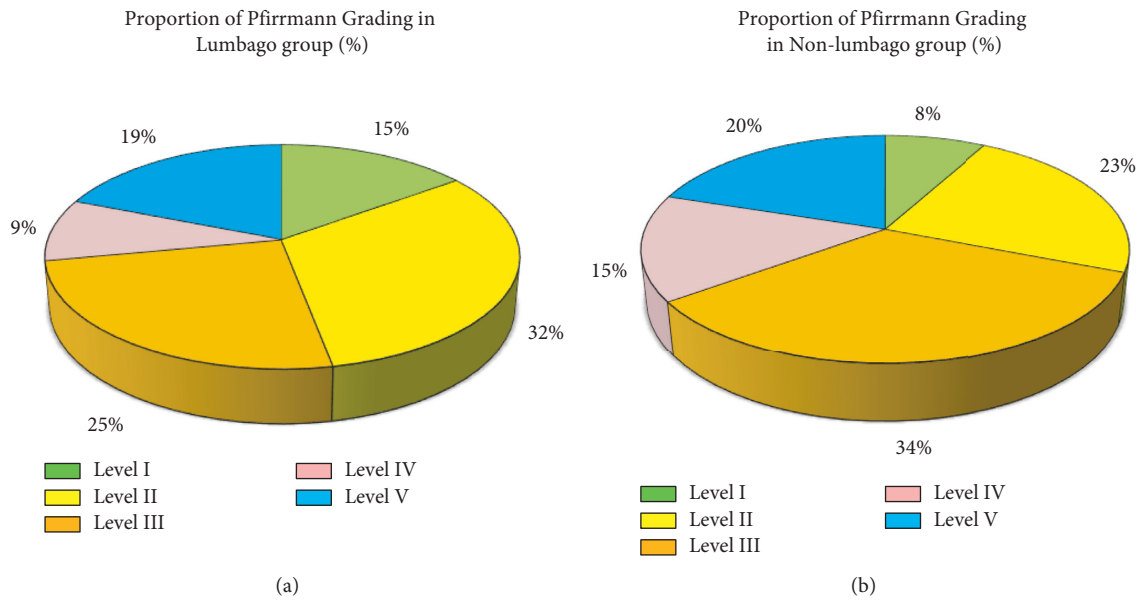

Figure 8: Degeneration degree of the intervertebral disc in different clinical symptoms. (a) Lumbago group; (b) nonlumbago group.

Table 3: The integrity of cartilage endplate and Pfirrmann grading distribution of intervertebral disc degeneration in the lumbago group.

	Pfirrmann grading					χ^2	P
	Level I	Level II	Level III	Level IV	Level V		
Complete	75	65	18	15	2	169.32	0.000
Partial disappearance	21	32	78	81	62		
Complete obliteration	4	3	4	4	36		

Table 4: The integrity of cartilage endplate and Pfirrmann grading distribution of intervertebral disc degeneration in the nonlumbago group.

	Pfirrmann grading					χ^2	P
	Level I	Level II	Level III	Level IV	Level V		
Complete	82	45	15	1	2	35.02	0.000
Partial disappearance	15	51	76	98	76		
Complete obliteration	3	4	8	1	22		

echo time and obtain images before the MR signal of short T2 tissue attenuates to 0 [23]. The cartilage endplate of intervertebral disc tissue is a kind of hyaline cartilage, rich in polysaccharides, collagen, and water. It shows no signal by conventional sequence, while UTE sequence can well display the cartilage endplate and short T2 tissue of the anterior and posterior longitudinal ligaments. In MR-UTE images, intact intervertebral discs and calcified cartilaginous endplates showed mainly medium-high signals near the cartilaginous endplate. In this study, Pfirrmann grades of T2WI sequences of patients with different degrees of disc degeneration were analyzed, and the results showed that there was little correlation between the disc degeneration degree and clinical symptoms, in line with the results of Sampara et al. [24].

Then, the morphological integrity of cartilage endplate in patients with and without lumbago was evaluated, which was divided into integrity, partial disappearance, and complete disappearance. The results showed that there was a statistical difference in the proportion of partial disappearance and complete disappearance of annulus fibrosus between the two groups ($P < 0.05$), indicating that low back pain was correlated with annulus fibrosus integrity. Next, the correlation between Pfirrmann grading and cartilage endplate integrity in two groups of patients with disc degeneration was analyzed, and the results showed that different degrees of disc degeneration were moderately correlated with cartilage endplate integrity, consistent with the results of Saberi et al. [25].

Finally, two groups of patients were compared for satisfaction with the nursing methods. The results showed that the patients in the lumbago group had good recovery effects, with high nursing satisfaction.

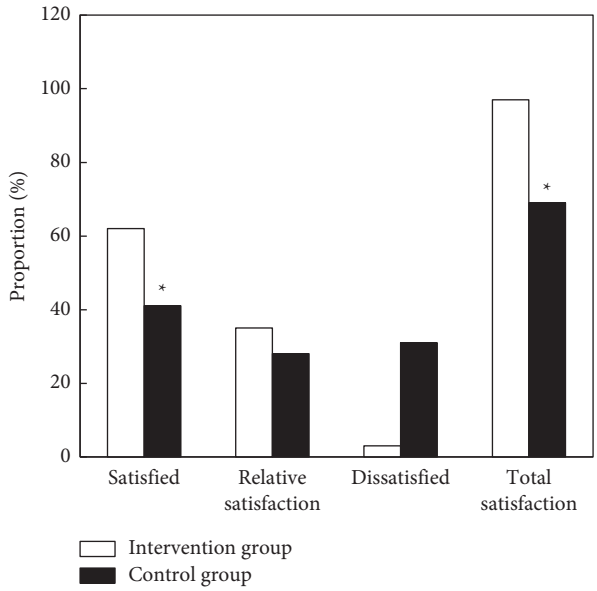

Figure 9: Comparison of rehabilitation nursing satisfaction. *Compared with the intervention group, $P < 0.05$.

5. Conclusion

In this study, MR-UTE imaging technology based on the CRN algorithm was used to analyze the images of 90 patients with intervertebral disc degeneration and to evaluate the therapeutic effect of rehabilitation nursing intervention. It was found that the CRN algorithm successfully removes artifacts and noise in the under-sampled image, that different degrees of intervertebral disc degeneration were moderately correlated with the integrity of cartilage endplate, and that cartilage endplate, annulus fibrosus, and bony endplate partially disappeared by the MR-UTE imaging technique. Rehabilitation intervention proved to have a positive effect on the treatment of patients with intervertebral disc degeneration and can improve patients' satisfaction. The limitation of this study is that the sample size is small, and the quality of MR-UTE data is different, which increases the evaluation error. Later, it is necessary to expand the sample size and include high-quality data for further in-depth discussion. In conclusion, MR-UTE imaging can clearly display the degeneration of disc cartilage, providing a new technique for the noninvasive evaluation of disc structure.

Data Availability

The data used to support the findings of this study are available from the corresponding author upon request.

Conflicts of Interest

The authors declare no conflicts of interest.

References

[1] J. Zhang, J. Zhang, Y. Zhang et al., "Mesenchymal stem cells-derived exosomes ameliorate intervertebral disc degeneration through inhibiting pyroptosis," *Journal of Cellular and Molecular Medicine*, vol. 24, no. 20, pp. 11742–11754, 2020.

[2] P. H. Wu, H. S. Kim, and I. T. Jang, "Intervertebral disc diseases part 2: a review of the current diagnostic and treatment strategies for intervertebral disc disease," *International Journal of Molecular Sciences*, vol. 21, no. 6, p. 2135, 2020.

[3] L. Kang, S. Liu, J. Li, Y. Tian, Y. Xue, and X. Liu, "The mitochondria-targeted anti-oxidant MitoQ protects against intervertebral disc degeneration by ameliorating mitochondrial dysfunction and redox imbalance," *Cell Proliferation*, vol. 53, no. 3, Article ID e12779, 2020.

[4] B. G. Ashinsky, E. D. Bonnevie, S. A. Mandalapu et al., "Intervertebral disc degeneration is associated with aberrant endplate remodeling and reduced small molecule transport," *Journal of Bone and Mineral Research*, vol. 35, no. 8, pp. 1572–1581, 2020.

[5] J. Lin, J. Zhuge, X. Zheng et al., "Urolithin A-induced mitophagy suppresses apoptosis and attenuates intervertebral disc degeneration via the AMPK signaling pathway," *Free Radical Biology and Medicine*, vol. 150, pp. 109–119, 2020.

[6] S. Veraa, W. Bergmann, I. D. Wijnberg et al., "Equine cervical intervertebral disc degeneration is associated with location and MRI features," *Veterinary Radiology & Ultrasound*, vol. 60, no. 6, pp. 696–706, 2019.

[7] U. Zehra, N. Noel-Barker, J. Marshall, M. A. Adams, and P. Dolan, "Associations between intervertebral disc degeneration grading schemes and measures of disc function," *Journal of Orthopaedic Research*, vol. 37, no. 9, pp. 1946–1955, 2019.

[8] W. Bergmann, N. Bergknut, S. Veraa et al., "Intervertebral disc degeneration in warmblood horses: morphology, grading, and distribution of lesions," *Veterinary Pathology Online*, vol. 55, no. 3, pp. 442–452, 2018.

[9] D. Nakashima, N. Fujita, J. Hata et al., "Quantitative analysis of intervertebral disc degeneration using Q-space imaging in a rat model," *Journal of Orthopaedic Research*, vol. 38, no. 10, pp. 2220–2229, 2020.

[10] Q. X. Zhang, D. Guo, F. C. Wang, and W. Y. Ding, "Necrosulfonamide (NSA) protects intervertebral disc degeneration via necroptosis and apoptosis inhibition," *European Review for Medical and Pharmacological Sciences*, vol. 24, no. 5, pp. 2683–2691, 2020.

[11] K. Ma, S. Chen, Z. Li et al., "Mechanisms of endogenous repair failure during intervertebral disc degeneration," *Osteoarthritis and Cartilage*, vol. 27, no. 1, pp. 41–48, 2019.

[12] L. Zhu, C. Yu, X. Zhang et al., "The treatment of intervertebral disc degeneration using traditional Chinese medicine," *Journal of Ethnopharmacology*, vol. 263, Article ID 113117, 2020.

[13] S. Senck, K. Trieb, J. Kastner, S. G. Hofstaetter, H. Lugmayr, and G. Windisch, "Visualization of intervertebral disc degeneration in a cadaveric human lumbar spine using microcomputed tomography," *Journal of Anatomy*, vol. 236, no. 2, pp. 243–251, 2020.

[14] K. Yang, H. Li, and C. Li, "Expression and role of Sphingosine 1-phosphate receptors in intervertebral disc degeneration," *Journal of Back and Musculoskeletal Rehabilitation*, vol. 33, no. 2, pp. 255–262, 2020.

[15] Z. Lv, L. Qiao, Q. Wang, and F. Piccialli, "Advanced machine-learning methods for brain-computer interfacing," *IEEE/ACM Transactions on Computational Biology and Bioinformatics*, vol. 18, no. 5, pp. 1688–1698, 2021.

[16] Z. Wan, Y. Dong, Z. Yu, H. Lv, and Z. Lv, "Semi-supervised support vector machine for digital twins based brain image fusion," *Frontiers in Neuroscience*, vol. 15, Article ID 705323, 2021.

[17] M. Hu, Y. Zhong, S. Xie, H. Lv, and Z. Lv, "Fuzzy system based medical image processing for brain disease prediction," *Frontiers in Neuroscience*, vol. 15, Article ID 714318, 2021.

[18] X. Zhou, Y. Li, and W. Liang, "CNN-RNN based intelligent recommendation for online medical pre-diagnosis support," *IEEE/ACM Transactions on Computational Biology and Bioinformatics*, vol. 18, no. 3, pp. 912–921, 2021.

[19] T. Oichi, Y. Taniguchi, K. Soma et al., "A mouse intervertebral disc degeneration model by surgically induced instability," *Spine 1976*, vol. 43, no. 10, pp. E557–E564, 2018.

[20] X. Zhou, T. Jin, L. Wang, E. Zhao, and X. Xiao, "Clinical practice of epidermal growth factor receptor-tyrosine kinase inhibitor targeted drugs combined with gadolinium oxide nanoparticles in the treatment of non-small cell lung cancer," *Bioengineered*, vol. 13, no. 1, pp. 128–139, 2022.

[21] C. Zhang, S. E. Gullbrand, T. P. Schaer et al., "Inflammatory cytokine and catabolic enzyme expression in a goat model of intervertebral disc degeneration," *Journal of Orthopaedic Research*, vol. 38, no. 11, pp. 2521–2531, 2020.

[22] K. Z. Lim, C. D. Daly, P. Ghosh et al., "Ovine lumbar intervertebral disc degeneration model utilizing a lateral retroperitoneal drill bit injury," *Journal of Visualized Experiments*, vol. 25, no. 123, Article ID 55753, 2017.

[23] Z. Li, X. Li, R. Tang, and L. Zhang, "Apriori algorithm for the data mining of global cyberspace security issues for human participatory based on association rules," *Frontiers in Psychology*, vol. 11, Article ID 582480, 2021.

[24] P. Sampara, R. R. Banala, S. K. Vemuri, G. R. Av, and S. Gpv, "Understanding the molecular biology of intervertebral disc degeneration and potential gene therapy strategies for regeneration: a review," *Gene Therapy*, vol. 25, no. 2, pp. 67–82, 2018.

[25] A. Saberi, Z. Salehi, B. Naderinabi, S. H. Ansari, and S. Mashayekhi, "Genetic dimension of intervertebral disc degeneration: polymorphism of matrix metalloproteinase 1 and 3 in the north Iranian population," *Turkish Neurosurgery*, vol. 28, no. 3, pp. 447–453, 2018.